PHYSICAL REVIEW C **101**, 044616 (2020)

Scale breaking in the low-energy proton-induced nonelastic cross sections

Masahiro Nakano,[1,2] Yuji Yamaguchi,[2] and Yusuke Uozumi[2]
[1] *Junshin Gakuen University, 1-1-1 Chikushigaoka, Minami-ku, Fukuoka 815-8510, Japan*
[2] *Department of Applied Quantum Physics and Nuclear Engineering, Kyushu University, 744 Motooka, Nishi-ku, Fukuoka 819-0395, Japan*

(Received 9 October 2019; accepted 30 March 2020; published 30 April 2020)

Proton-induced nonelastic cross sections for ^{12}C, ^{27}Al, ^{56}Fe, and ^{208}Pb are investigated in a low-energy region below 100 MeV down to nearly 0 MeV based on a framework of an intranuclear cascade (INC) model. We point out that there is a scaling among the calculations including the Coulomb repulsion; two cases are shown: One is the scaling of the trajectories with different impact parameters, and the other is the incident-energy dependence of the cross sections. We point out for the first time that the calculated cross sections by the usual INC model follow a scaling and the discrepancy between the calculated cross sections and the experimental data indicates the scale breaking and that, for the explanation of the scale breaking, it is essential to include the discrete level constraints in addition to the Coulomb repulsion in the INC model.

DOI: 10.1103/PhysRevC.101.044616

I. INTRODUCTION

The nonelastic cross section is one of the most important physical quantities defined as the total cross section minus the elastic-scattering cross section. It includes all the reactions, such as particle emissions, inelastic scatterings, and absorptions except the elastic scattering. Concerning the proton-induced nonelastic cross sections, the experimental data are shown in Fig. 1 for ^{12}C, ^{27}Al, ^{56}Fe, and ^{208}Pb where the nonelastic cross sections are relatively well measured [1–23]. Although the data have experimental errors, the tendencies of the cross sections can be recognized.

For the nucleon-induced reactions, there are several dynamic models, such as the intranuclear cascade model [24], quantum molecular dynamics [25], and antisymmetrized molecular dynamics [26]. Among them, the intranuclear cascade (INC) model is a remarkable approach to the nuclear reactions. As examples, the extensive studies based on the Liege INC model have succeeded to explain various experimental data not only for nucleon-induced reactions, but also for antiproton, pion, and light cluster-induced reactions, and they have shown the INC model can apply various phenomena [27–30]. In addition, the Uozumi group have shown that their INC model followed by the generalized evaporation model [31] has explained various reactions, such as (p, p'x), (p, dx), and (p,αx) in very wide energies and angles [32–35].

In this paper, we investigate the proton-induced nonelastic cross sections in the low-energy region below 100 MeV. Concerning on the proton-induced nonelastic cross sections, the INC of the Liege group reproduce the experimental data in medium- and high-energy regions, however, there are no calculations which reproduce the experimental nonelastic cross sections in the very low-energy region [27,28].

In our previous paper, we have discussed neutron-induced nonelastic cross sections in the low-energy region below 100 MeV [36], and we have shown for the first time that the introduction of "discrete level constraints" (DLC) is essential to explain the neutron-induced nonelastic cross sections in the very low energy. However, for the proton-induced nonelastic cross sections, it is difficult to verify the existence of the discrete level constraint since there is the effect of Coulomb repulsion which brings a similar incident-energy dependence in the cross sections. The incident proton is ruled by the Coulomb potential, then, it has been generally believed that the proton-induced nonelastic cross sections can be explained only by the effect of the Coulomb repulsion. The important problem is whether the Coulomb repulsion is enough to reproduce the experimental data or not. In this paper, we investigate this problem precisely using the scaling in the usual INC calculations.

The purposes of this paper are, first, to show a scaling in two different ways; one is a scaling in the trajectories of the injected proton, and the other is a scaling among the cross sections given by the usual INC calculations including the Coulomb repulsion and the nuclear potential. Second, to show the scale breaking which indicates a discrepancy between the experimental data and the INC calculations. Finally, to show that the scale breaking is explained by the INC calculation including the effects of discrete level constraints in addition to the Coulomb potential.

II. INTRANUCLEAR CASCADE MODEL

In the INC model, the position and momentum of the particles in the ground state is prepared based on a random sampling for every injection of the nucleon. We will not repeat how to make the ground state since the method of making the ground state is described in Ref. [36].

On the two-body interactions, there have been the two-body cross sections introduced by Cugnon *et al.* [37], who proposed the following Eqs. (1) and (2) to reproduce the free nucleon-nucleon cross sections. The two-body cross sections

S^{free} (mb) are expressed for each energy interval:

$$\begin{array}{ll}
\text{for } pp, & \\
S^{\mathrm{free}} = 41 + 60(P_G - 0.9)\exp(-1.2P_G) & \text{for } 1.5\ \mathrm{GeV}/c < p_G < 5\ \mathrm{GeV}/c, \\
S^{\mathrm{free}} = 23.5 + 24.6/\{1 + \exp[-(P_G - 1.2)/0.1]\} & \text{for } 0.8\ \mathrm{GeV}/c < p_G < 1.5\ \mathrm{GeV}/c, \\
S^{\mathrm{free}} = 23.5 + 1000(P_G - 0.7)^4 & \text{for } 0.4\ \mathrm{GeV}/c < p_G < 0.8\ \mathrm{GeV}/c, \\
S^{\mathrm{free}} = 34(P_G/0.4)^{-2.104} & \text{for } p_G < 0.4\ \mathrm{GeV}/c
\end{array} \tag{1}$$

$$\begin{array}{ll}
\text{for } np, & \\
S^{\mathrm{free}} = 42 & \text{for } p_G > 2\ \mathrm{GeV}/c, \\
S^{\mathrm{free}} = 24.2 + 8.9P_G & \text{for } 1\ \mathrm{GeV}/c < p_G < 2\ \mathrm{GeV}/c, \\
S^{\mathrm{free}} = 33 + 196[abs(P_G - 0.95)]^{2.5} & \text{for } 0.4\ \mathrm{GeV}/c < p_G < 1\ \mathrm{GeV}/c, \\
S^{\mathrm{free}} = 6.3555{P_G}^{-3.2481}\exp[-0.377(\ln\ P_G)^2] & \text{for } p_G < 0.4\ \mathrm{GeV}/c,
\end{array} \tag{2}$$

where p_G is the relative momentum of the two nucleons in the unit of GeV$/c$.

On the other hand, we introduced a new set of two-body cross sections S (mb) so as to reproduce the nonelastic cross sections. For the calculations of ^{12}C, ^{27}Al, ^{56}Fe, and ^{208}Pb, we used the same two-body cross sections. The formula is given for $p_G < 5\,\mathrm{GeV}/c$ in Eqs. (3) and (4). Note that the expression is not unique since many formulas can represent a similar shape

$$\begin{aligned}
&\text{for}\quad pp,\\
&S = Y1 + Y2,\\
&Y1a = 29/\{1 + \exp[-(p_G - 1.26)/0.06]\} + 19.5,\\
&Y1b = 41 + 60(p_G - 0.9)\exp(-1.2p_G),\\
&Y1 = Y1a/(1 + \exp((p_G - 1.5)/0.5))\\
&\qquad + Y1b/(1 + \exp(-(p_G - 1.5)/0.5)),\\
&Y2 = 825\ \exp\left(-p_G^{0.8}/0.07\right) + 20\,000\ \exp\left(-p_G^{0.86}/0.02\right),
\end{aligned} \tag{3}$$

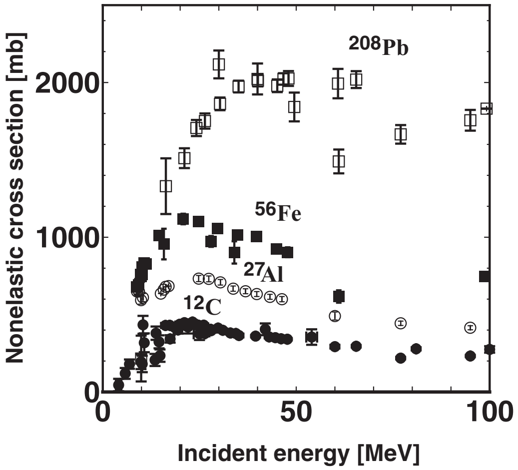

FIG. 1. Experimental data of proton-induced nonelastic cross sections of ^{12}C (dots), ^{27}Al (circles), ^{56}Fe (boxes), and ^{208}Pb (squares) with error bars. The x axis represents the incident energy (MeV) of the injected proton, and the y axis represents the nonelastic cross section (mb). The experimental data were taken for ^{12}C from Refs. [1–9], for ^{27}Al from Refs. [4,5,8,10–12], for ^{56}Fe from Refs. [12–20], and for ^{208}Pb from Refs. [6,8,18,19,21–23]. The same experimental data are used in Figs. 5, 9, and 11.

$$\begin{aligned}
&\text{for}\quad np,\\
&S = Y1 + Y2,\\
&Y1a = (10p_G + 23)\{1 + 0.2\ \exp[-(p_G - 0.5)/0.15]\},\\
&Y1b = 42/\{1 + \exp[-(p_G - 1.93)/0.05]\},\\
&Y1 = Y1a/\{1 + \exp[(p_G - 1.93)/0.05]\} + Y1b\\
&Y2 = 3200\ \ \exp(-p_G/0.064)\\
&\qquad \times\{1 - 0.3\ \exp[-(p_G - 0.3)^2/0.2]\}.
\end{aligned} \tag{4}$$

Comparisons between the two sets of the two-body cross sections are shown in Fig. 2. The x axis represents the incident particle energy T_{lab} (MeV) in the laborarory frame. The relation between T_{lab} and p_G in the relativistic calculation is given using the nucleon mass$M$ as follows:

$$T_{\mathrm{lab}} = \sqrt{{P_G}^2 + M^2} - M. \tag{5}$$

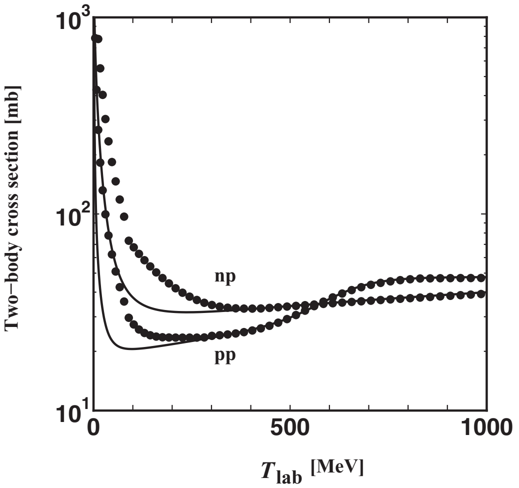

FIG. 2. Comparison of two-body cross sections between the Cugnon *et al.* (dotted curves) and the proposed one (solid curves) used in this calculation. The x axis is the kinetic energy T_{lab} (MeV), and the y axis is the two-body cross section (mb).

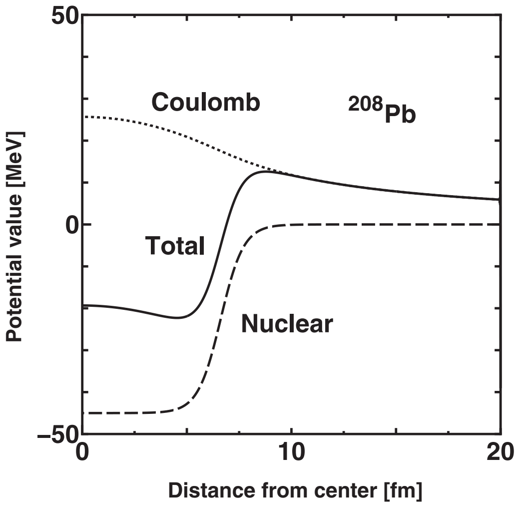

FIG. 3. Potentials for ^{208}Pb. The dotted curve indicates the Coulomb potential of the finite-size charge distribution, the dashed curve is the nuclear potential of the Woods-Saxon shape, and the solid curve shows the total of the two potentials which is used in this calculation. The x axis is the radius (fm), and the y axis is the potential energy (MeV).

It is reasonable to use different parametrizations in this calculation. The Cugnon *et al.* parametrization of two-body cross sections has been determined to reproduce the free pp and pn cross sections. On the other hand, our parametrization is determined to obtain a better description of the experimental data on a many-body system where the "in-medium" interactions should be essential. When we use the parameters of Cugnon *et al.*, the calculations largely overestimate the experimental data. As a result, our two-body cross sections are smaller than those by Cugnon *et al.* below 400 MeV as shown in Fig. 2.

III. RESULTS AND DISCUSSIONS

A. Effect of the Coulomb repulsion

The potentials for ^{208}Pb as an example are shown in Fig. 3. The Coulomb potential for finite-size charge is different from the point charge potential, and it is given by the dotted curve, the nuclear potential of the Woods-Saxon shape is given by the dashed curve, and the sum of the two potentials is the solid curve. In this calculation, the charge distribution is taken as the same Woods-Saxon shape as the density, thus, there are no further parameters. The potentials for four targets which affect the proton trajectory are shown in Fig. 4. The figures give the maximum values of the potentials, so-called "the height of the Coulomb barrier." The height of Coulomb barrier $V_{\max}$ and the location $r_{\max}$ are summarized in Table I.

From Fig. 4, we can note the height of the Coulomb barrier for ^{12}C is very small, on the contrary, the height for ^{208}Pb is large. Since the Coulomb interaction has the long-range tail, the calculation should be performed from a very far distance for keeping the precision of the calculations. The start point in our calculation is $Z = -1000$ fm

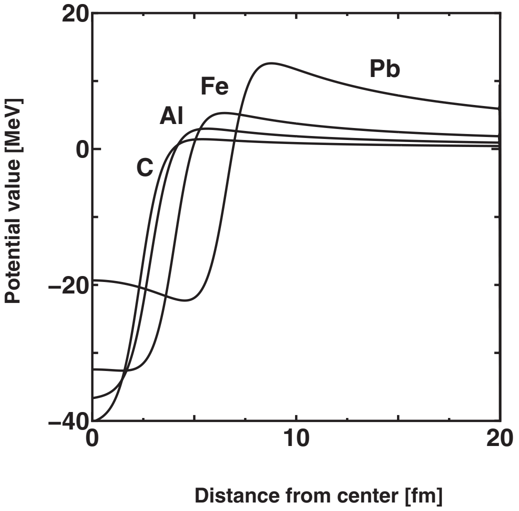

FIG. 4. The total potentials for ^{12}C, ^{27}Al, ^{56}Fe, and ^{208}Pb which sum the Coulomb potentials of the finite-size charge and the nuclear potentials.

The result by the INC calculation with the Coulomb plus nuclear potential is shown in Fig. 5. There is a large discrepancy in ^{12}C and a little difference in ^{27}Al as shown in Fig. 5. We can note two facts; one is the cross sections for the light nuclei ^{12}C and ^{27}Al are large compared with the experimental data. The second is that the shapes of the rising in the low-energy region below 10 MeV are different in the light nuclei, especially in the target 12C as shown in Fig. 5. In the next section, we show that the reason for this discrepancy relates with the scale breaking in the calculated cross sections and the experimental data.

B. Scaling in the Coulomb repulsion

In the case of the point charge, the Rutherford scattering for the proton by the Coulomb repulsion has a scaling law since the cross section is proportional to the quantity T_{lab}/Z. Similar to the point charge scattering, we can confirm that there is a scaling in the finite-size charge when we take the ratio $T_{\mathrm{lab}}\ /V_{\max}$. The factor of $T_{\mathrm{lab}}\ //V_{\max}$ is the ratio of the incident energy to the Coulomb height and a good measure of the proton's incident energy against the Coulomb repulsive potential in the finite-size charge distribution. We call the ratio the scaled incident energy. The ratio is a nondimensional quantity. We show two cases where the scaled incident energy controls the phenomena.

First, we show the scaling on the trajectories of the injected proton, taking an example of the pair of ^{12}C and ^{208}Pb. The

TABLE I. Height $V_{\max}$ of the Coulomb barrier and its radius $r_{\max.}$. for ^{12}C, ^{27}Al, ^{56}Fe, and ^{208}Pb.

	C	Al	Fe	Pb
$r_{\max.}$ (fm)	5.39	5.62	6.48	8.78
$V_{\max}$ (MeV)	1.44	2.99	5.28	12.59

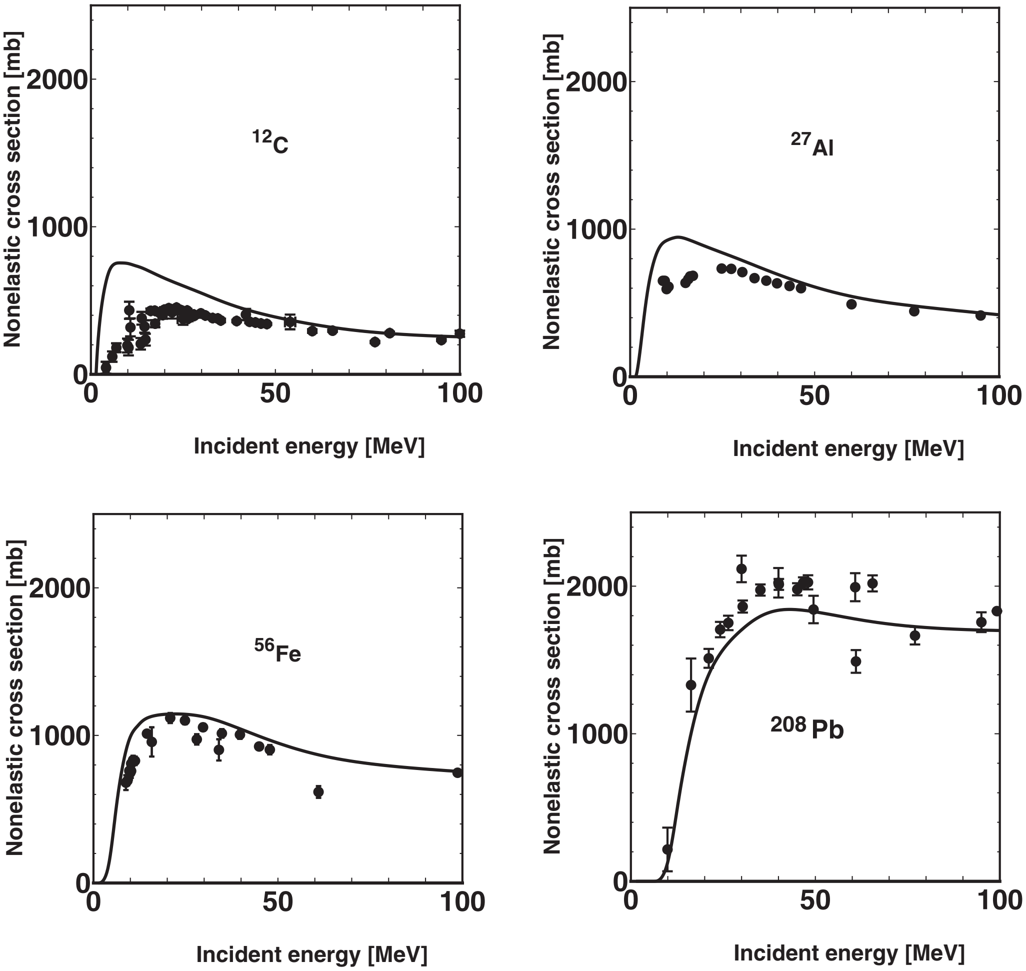

FIG. 5. Comparison of the usual INC calculations (solid curves) and the proton-induced nonelastic cross sections for ^{12}C, ^{27}Al, ^{56}Fe, and ^{208}Pb (dots). The INC calculations, here, include the Coulomb and nuclear potentials.

Coulomb repulsion bent outward the trajectries of the injected proton, and the proton-induced cross sections are reduced as a result. We directly checked the scaling by comparing the trajectries of the impact parameters from 1 to 10 (fm) solving the only potential scattering (not full INC calculation) under the total potentials of the Coulomb and nuclear potentials. The cases having the same scaled incident energies for ^{208}Pb and for ^{12}C should be compared in Figs. 6 and 7. The calculated trajectories clearly show the existence of the scaling with the scaling factor of $T_{\text{lab}}/V_{\max}$. The trajectories running outside the nucleus of ^{12}C are similar to the trajectories in ^{208}Pb in the pairs of the incident energies with the same ratios of the Coulomb barriers. Note that the trajectories running inside the nucleus are different from each other since the nuclear potentials have no clear scaling.

Next, we show the most impotrant case, i.e., the scaling in the calculated cross sections in Fig. 5, which are given by the usual INC model with the Coulomb repulsion and nuclear potential shown. We point out that these calculated cross sections have a scaling of the quantity $T_{\text{lab}}\,/V_{\max}$, i.e., scaled incident energy, for four targets. The scaling, in this case, means that the incident energy dependence of the cross sections is same for the same scaled incident energy. Note that the absolute values of the cross sections are not the same since the target sizes are different from each other. The scaled incident energy dependence of the calculated cross sections in Fig. 5 is illustrated in Fig. 8. The result shown in Fig. 8 indicates that the INC calculations follow approximately a scale when the Coulomb and nuclear potentials are included. However, when we look at the experimental data in the scaled incident energy, we note that there is not such a scaling as is shown in Fig. 9. If the experimental data follow the scaling, the shape of the scaled incident energy dependence should be similar to the sharp rising shape as in Fig. 8. However, the shape of the scaled incident energy dependence of the cross sections of ^{12}C is slow rising and completely different from those of ^{208}Pb. This discrepancy indicates that the scaling in experimental data breaks down contrary to the usual INC calculations. It is evident that the scaled calculations with the Coulomb force cannot explain this nonscaled experimental data. In the next section, we point out that this discrepancy can be resolved by the DLC.

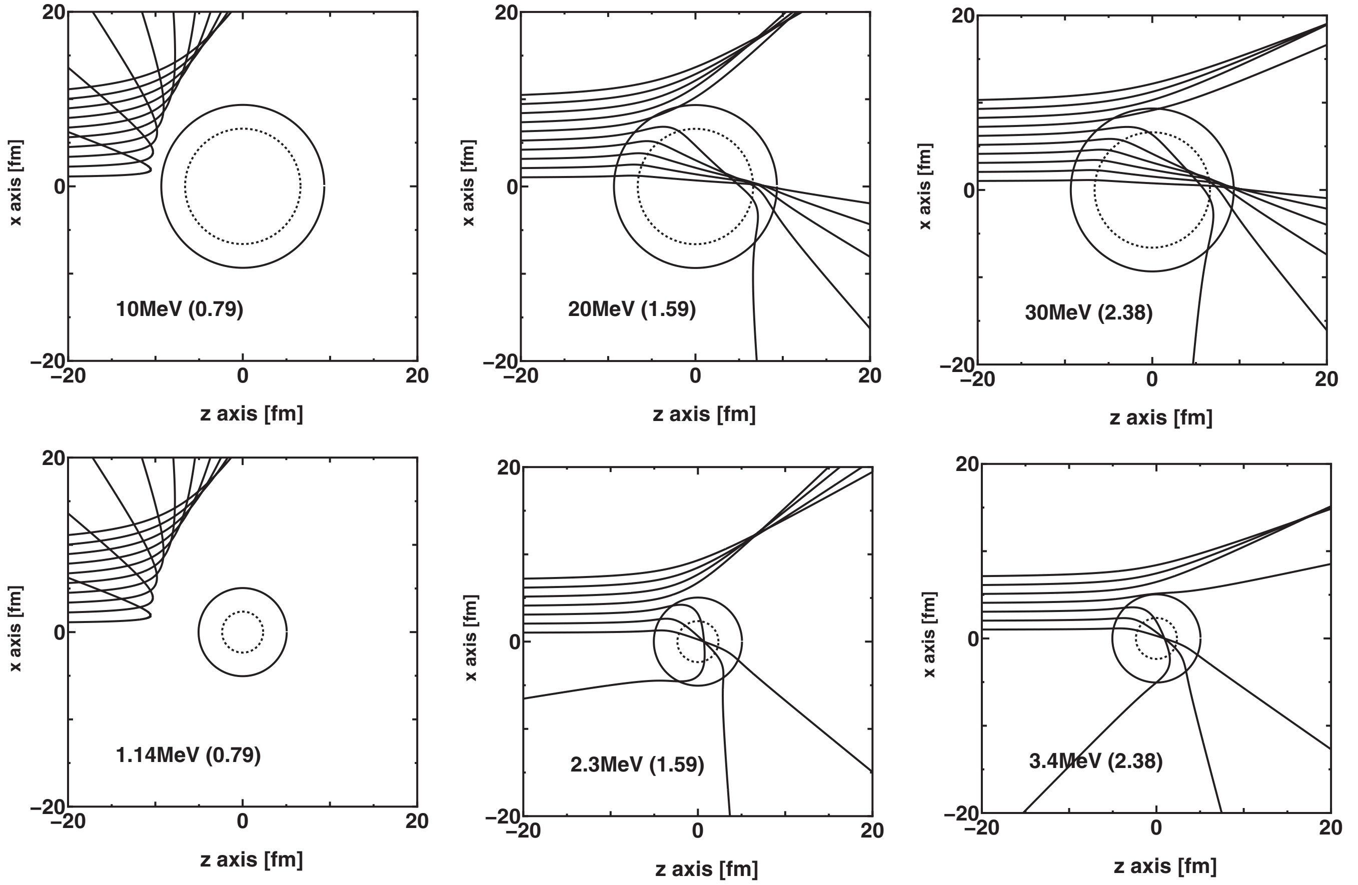

FIG. 6. Trajectories of the impact parameter from 1 to 10 (fm) on a two-dimensional plane under the only potential scattering (not full INC calculation). The above three figures show the trajectories of the ^{208}Pb target for energies $T_{\text{lab}} = 10$, 20, and 30 MeV. The lower three figures show the cases for the ^{12}C target for energies $T_{\text{lab}} = 1.14$, 2.3, and 3.4 MeV. The pair of figures of up and down have the same scaled incident energies $T_{\text{lab}}/V_{\text{max}}$ which are shown in the parentheses. The dotted circles show the radius r_0 of the Woods-Saxon potential, and the solid circles show the radius of the maximum height of the total potential (r_{max} in Table I).

C. Effects of the discrete level constraints

The naive INC model assumes that the levels are continuum over the Fermi energy. This assumption is not proper. In principle, the particles having a very low energy should lead to the target excitations of discrete levels. The allowed phase space of the excitations is going to zero when the particle energy goes to zero. In order to include this effect, we have introduced the discrete level constraints in the previous paper [36], which is essential for the neutron-induced nonelastic cross sections. Similar to the neutron case, the discrete level constraints should be included for the proton-induced reactions. We follow the same formulation as the neutron-induced reactions [36].

The transition in energy of the scattered two particles is

$$E1 + E2 \rightarrow E1' + E2'. \tag{6}$$

The transition probability of the scattered nucleon is given by the probability $P(E)$. In this paper, we simplify the probability by introducing the following shape, which is considered an average over the probabilities to several discrete levels with widths:

$$P(E) = 1/\{1 + \exp[-(E_0 - E)/w]\}. \tag{7}$$

The function of $P(E)$ is called a sigmoid curve, which is a smooth curve from 0 to 1. As shown in Fig. 10, the probability $P(E)$ approaches 0 as E goes to Ed (Fermi energy) and to 1 as E goes to Eu (free energy). For the parameters in Eq. (7), we set E_0 as a slightly larger value than the half point of Ed and Eu, and $w = 1.2$ MeV. The parameters E_0 listed in Table II have little target dependence. It is noted that the essential feature of the shape does not largely depend on the detail of the parameters. We require that both nucleons having the energies $E1'$ and $E2'$ follow the probability distribution $P(E1')$ and $P(E2')$ as a whole. The process is forbidden when the two nucleon transitions do not follow the transition probability. It should be stressed that this condition is different from the Pauli blocking which is generally used. The Pauli blocking condition works for nucleons in the energy range of $E < E_{\text{Fermi}}$, on the other hand, the discrete level constraints do in the energy range of $E > E_{\text{Fermi}}$.

The resultant cross sections of the full INC calculations including the discrete level constraints in addition to the Coulomb repulsion are compared with the experimental data in Fig. 11. The result indicates the simple treatment of discrete level constraints works well. Using the results of these calculations, we can make the scaled cross sections

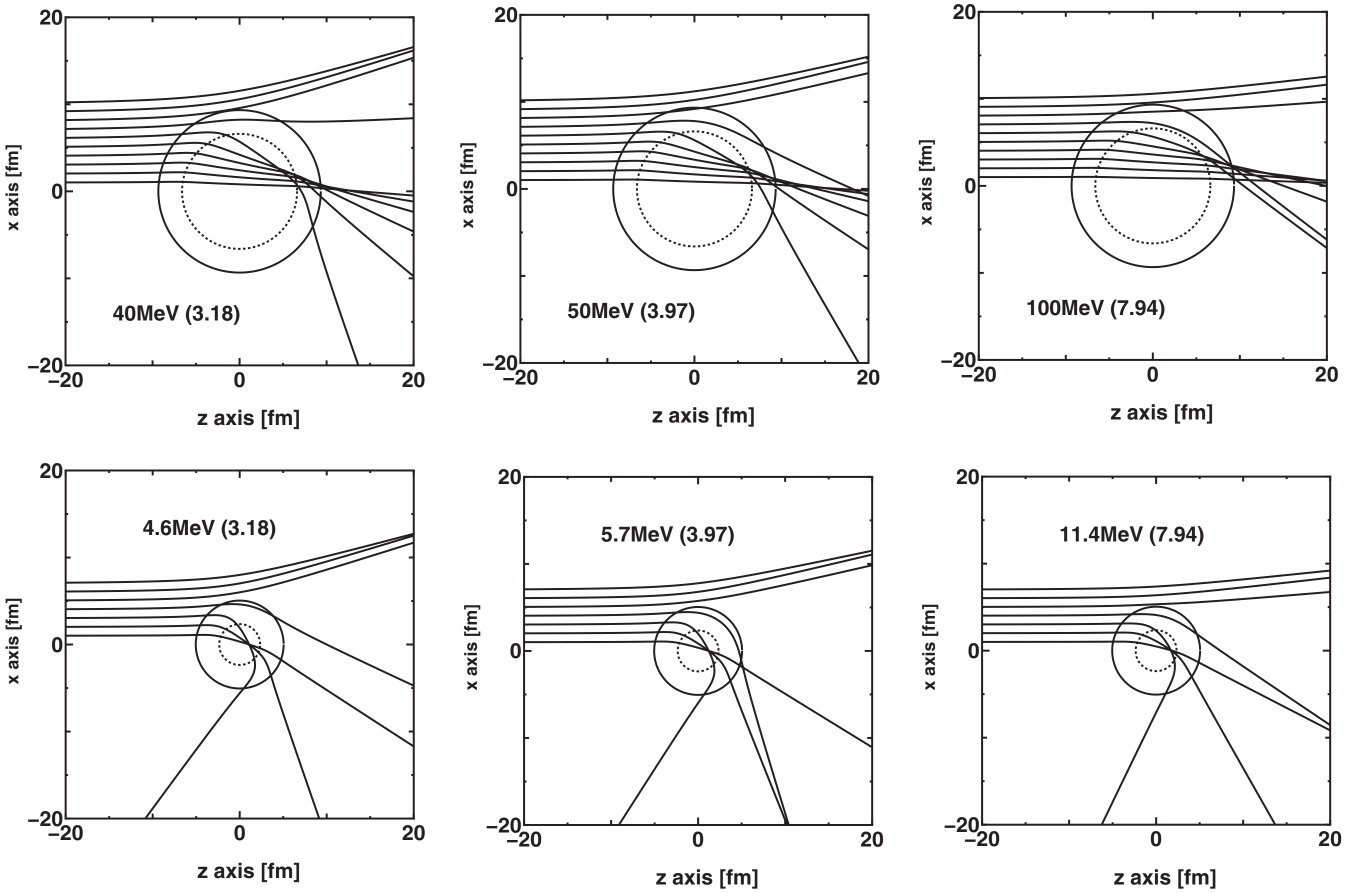

FIG. 7. Trajectories of different impact parameters on a two-dimensional plane of the unit (fm). The above three figures show the trajectories for the ^{208}Pb target. The lower three figures show the cases for the ^{12}C target with the same scaled incident energies. The meaning of the lines and numbers is the same as Fig. 6.

just as in Fig. 8. As is shown in Fig. 12, the result clearly indicates the full INC calculations break down the scaling largely in ^{12}C and slightly in ^{27}Al. This fact indicates the discrete level constraints resolve the discrepancy between the

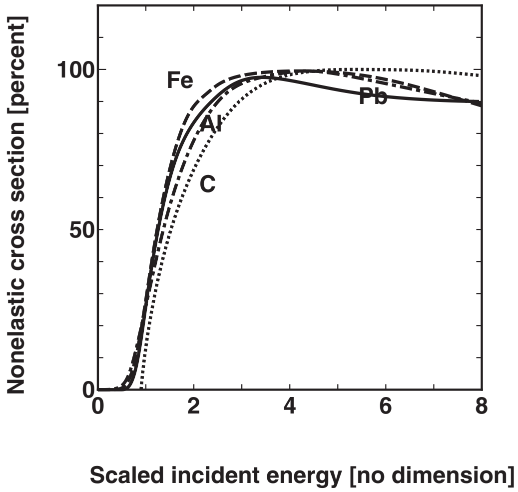

FIG. 8. Scaled cross sections of calculations in Fig. 5. The *x* axis is $T_{\text{lab}}/V_{\max}$, which is the scaled incident energies with no dimension. The factor $V_{\max}$ is listed in Table I for ^{12}C, ^{27}Al, ^{56}Fe, and ^{208}Pb. For comparison, the values of the cross sections are normalized so that the maximum value is 100%.

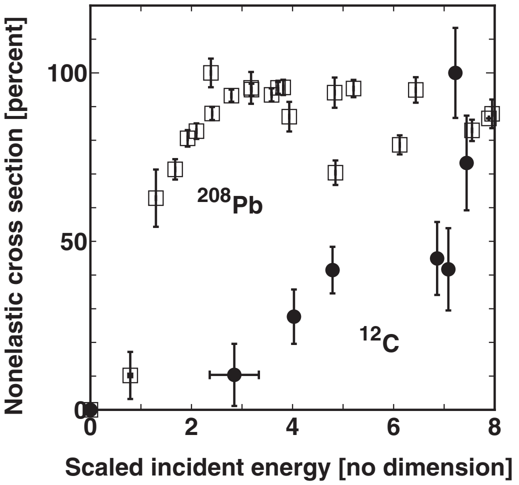

FIG. 9. Scaled experimental proton-induced nonelastic cross sections of ^{12}C (dots) and ^{208}Pb (squares) where the *x* axis represents the scaled incident energy $T_{\text{lab}}/V_{\max}$ (dimensionless). The experimental data are the same as in Fig. 1, however, the *x* and *y* axes are scaled the same way as in Fig. 8.

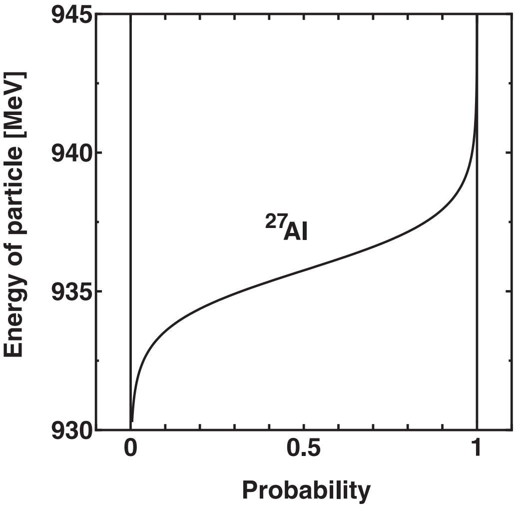

FIG. 10. An example of the transition probability $P(E)$ used in our calculations. The x axis indicates the probability from 0 to 1 for the energy of the scattered particle in the y axis.

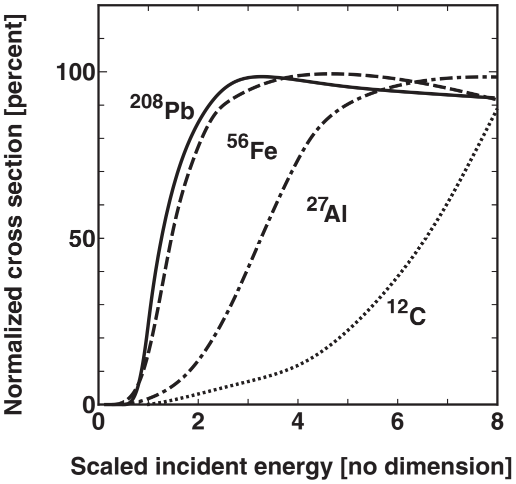

FIG. 12. Scaled cross sections of Fig. 11 given by full INC calculations including both effects of discrete level constraints and Coulomb repulsion. The x and y axes are scaled as the same way as in Fig. 8.

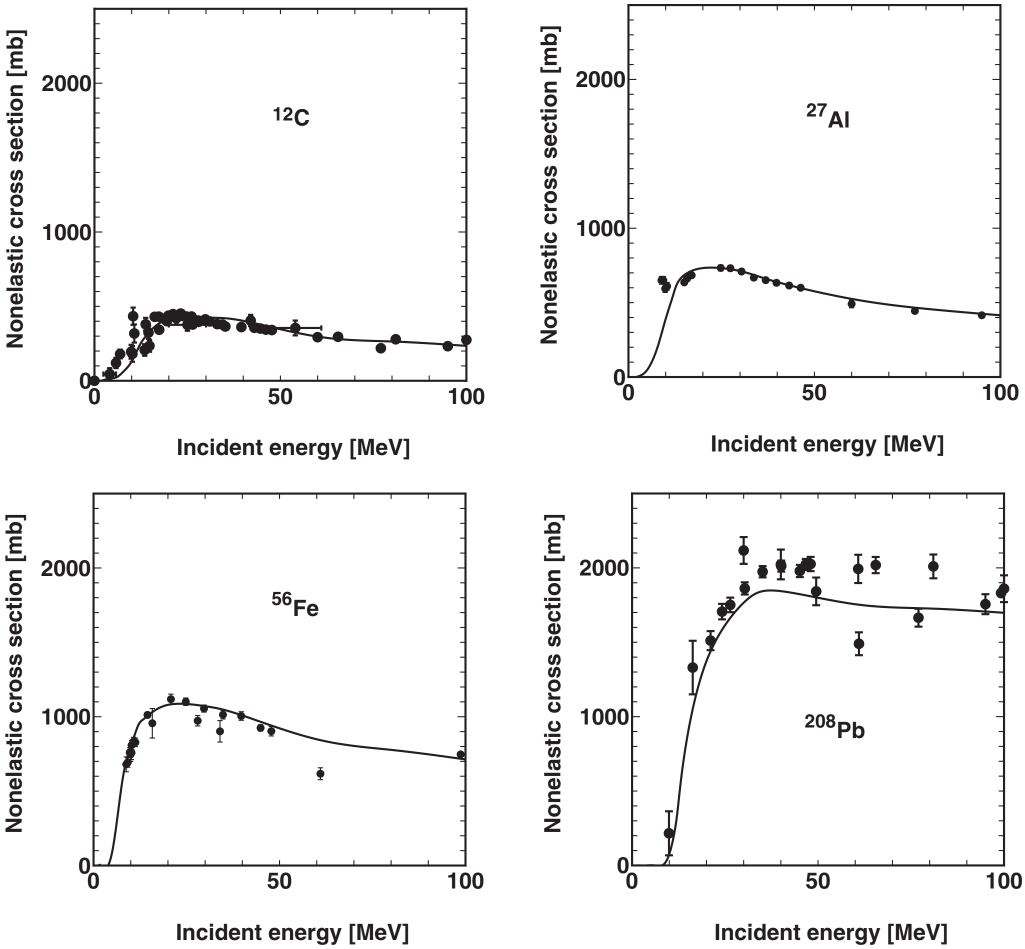

FIG. 11. Comparison of the new INC calculations (solid curves) with the proton-induced nonelastic cross sections for ^{12}C, ^{27}Al, ^{56}Fe, and ^{208}Pb (dots). The new INC calculations, here, further include the DLC effects in addition to the Coulomb and the nuclear potentials, which are included in the calculations in Fig. 5. The experimental data are the same as in Fig. 1, and the meaning of the x and y axes are also the same as in Fig. 1

TABLE II. List of E_0 (MeV) for four targets and for the proton or neutron of the scattered particle.

	C	Al	Fe	Pb
Neutron	940	938	936	936
Proton	941	940	938	938

calculations and the experimental data and explain the scale breaking.

IV. CONCLUSIONS

We have investigated the proton-induced nonelastic cross sections in the low-energy region below 100 MeV. The most important conclusion is that, for an explanation of scale breaking in the experimental cross sections, we should introduce the discrete level constraints as the neutron-induced nonelastic cross sections.

We have shown that the calculations with only Coulomb repulsion have the scaling. On the other hand, the experimental data break the scaling since there is the discrepancy with the scaled calculations. These facts indicate that only the Coulomb repulsion cannot reproduce the experimental data especially for light nuclei ^{12}C and ^{27}Al.

In order to resolve the discrepancy, we introduced the DLC for the calculations of proton-induced cross sections. The introduction of the DLC has been proved to be essential for neutron-induced nonelastic cross sections [36]. In the proton injections, we also showed the INC model including the discrete level constraints in addition to the Coulomb repulsion can reproduce the experimental data in the four nuclei ^{12}C, ^{27}Al, ^{56}Fe, and ^{208}Pb. It should be noted that, since the effects of discrete level constraints are confined to the very low energy and the light targets, it has been difficult to find out the effects of the discrete level constraints from the experiment data especially in the heavy nuclei, such as ^{208}Pb.

We add a comment on the transition probability function. The usage of the continuous sigmoid function for the transition probability is not universal. It should be considered as a simple procedure. The sigmoid function is used to correspond to the general feature that the discrete levels are few in the low excitation energy region and are many in the high excitation energy region.

As a summary, we pointed out for the first time the following three facts. First, there exists an approximate scaling among the cross sections given by the usual INC including only Coulomb repulsion. Second, the experimental data break the scaling. Third, in order to explain the scale breaking, it is crucial to introduce the effect of discrete level constraints besides the Coulomb potential, then the INC can reproduce the proton-induced nonelastic cross sections in the wide range of targets and in the energy range from 100 MeV down to nearly 0 MeV.

ACKNOWLEDGMENTS

We acknowledge Dr. G. Watanabe and the members of the Uozumi group of Kyushu University for constructive comments and encouragement during the course of this work.

[1] J. F. Dicello and G. Igo, Phys. Rev. C **2**, 488 (1970).
[2] M. Q. Makino, C. N. Waddell, and R. M. Eisberg, Nucl. Phys. **68**, 378 (1965).
[3] R. A. Ciles and E. J. Burge, Nucl. Phys. **50**, 327 (1964).
[4] W. F. McGill, R. F. Carlson, T. H. Short, J. M. Cameron, J. R. Richardson, I. Šlaus, W. T. H. van Oers, J. W. Verba, D. J. Margaziotis, and P. Doherty, Phys. Rev. C **10**, 2237 (1974).
[5] J. J. H. Menet, E. E. Gross, J. J. Malanify, and A. Zucker, Phys. Rev. Lett. **22**, 1128 (1969).
[6] A. Ingemarsson, J. Nyberg, and P. U. Renberg *et al.*, Nucl. Phys. A **653**, 341 (1999).
[7] A. Auce, A. Ingemarsson, R. Johansson, M. Lantz, G. Tibell, R. F. Carlson, M. J. Shachno, A. A. Cowley, G. C. Hillhouse, N. M. Jacobs, J. A. Stander, J. J. van Zyl, S. V. Förtsch, J. J. Lawrie, F. D. Smit, and G. F. Steyn, Phys. Rev. C **71**, 064606 (2005).
[8] R. Goloskie and K. Strauch, Nucl. Phys. **29**, 474 (1962).
[9] J. B. Edward, Nucl. Phys. **13**, 511 (1959).
[10] N. Okumura, Y. Aoki, and T. Joh *et al.*, Nucl. Instrum. Methods Phys. Res., Sect. A **487**, 565 (2002).
[11] K. Bearpark, W. R. Graiiam, and G. Jones, Nucl. Phys. **73**, 206 (1965).
[12] P. J. Bulman, G. W. Greenlees, and M. J. Sametband, Nucl. Phys. **69**, 536 (1965).
[13] J. F. Dicello, G. J. Igo, and M. L. Roush, Phys. Rev. **157**, 1001 (1967).
[14] C. Hojvat and G. Jones, Nucl. Instrum. Methods **66**, 13 (1968).
[15] R. H. Mccamis, N. E. Davison, and Van W. T. H *et al.*, Can. J. Phys. **64**, 685 (1986).
[16] M. Q. Makino, C. N. Waddell, and R. M. Eisberg *et al.*, Phys. Lett. **9**, 178 (1964).
[17] T. J. Gooding, Nucl. Phys. **12**, 241 (1959).
[18] V. Mever, R. M. Eisberg, and R. F. Carlson, Phys. Rev. **117**, 1334 (1960).
[19] P. Kirkby and W. T. Link, Can. J. Phys. **44**, 1847 (1966).
[20] B. D. Wilkins and G. Igo, Phys. Rev. **129**, 2198 (1963).
[21] R. E. Pollock and G. Schrank, Phys. Rev. **140**, B575 (1965).
[22] R. F. Carlson, A. J. Cox, J. R. Nimmo, N. E. Davison, S. A. Elbakr, J. L. Horton, A. Houdayer, A. M. Sourkes, W. T. H. van Oers, and D. J. Margaziotis, Phys. Rev. C **12**, 1167 (1975).
[23] J. J. H. Menet, E. E. Gross, J. J. Malanify, and A. Zucker, Phys. Rev. C **4**, 1114 (1971).
[24] R. Serber, Phys. Rev. **72**, 1114, (1947).
[25] J. Aichelin and H. Stocker, Phys. Lett. B **176**, 14 (1986).
[26] A. Ono, H. Horiuchi, T. Maruyama, and A. Ohnishi, Prog. Theor. Phys. **87**, 1185 (1992).
[27] A. Boudard, J. Cugnon, J. C. David, S. Leray, and D. Mancusi, Phys. Rev. C **87**, 014606(2013).
[28] J. L. Rodríguez-Sánchez, J.-C. David, D. Mancusi, A. Boudard, J. Cugnon, and S. Leray, Phys. Rev. C **96**, 054602 (2017).
[29] J. Cugnon, A. Boudard, J. C. David, S. Leray, and D. Mancusi, EPJ Web Conf. **66**, 03021 (2014).

[30] J. Cugnon, T. Aoust, A. Boudard, J. C. David, S. Pedoux, S. Leray, and Y. Yariv, Adv. Space Res. **40**, 1332 (2007).

[31] S. Furihata and T. Nakamura, J. Nucl. Sci. Technol. **39**, 758 (2002).

[32] Y. Uozumi, Y. Sawada, A. Mzhavia, S. Nogamine, H. Iwamoto, T. Kin, S. Hohara, G. Wakabayashi, and M. Nakano, Phys. Rev. C **84**, 064617 (2011).

[33] Y. Uozumi, T. Yamada, S. Nogamine, and M. Nakano, Phys. Rev. C **86**, 034610 (2012).

[34] Y. Uozumi, T. Yamada, and M. Nakano, J. Nuc. Sci. Technol. **52**, 264 (2015).

[35] Y. Uozumi, Y. Yamaguchi, G. Watanabe, Y. Fukuda, R. Imamura, M. J. Kobra, and M. Nakano, Phys. Rev. C **97**, 034630 (2018).

[36] M. Nakano and Y. Uozumi, Phys. Rev. C **100**, 034619 (2019).

[37] J. Cugnon, D. L. Hote, and J. Vandermeulen, Nucl. Instrum. Methods Phys. Res, Sect. B **111**, 215 (1996).